Chinese Chemical Letters 36 (2025) 110789

Contents lists available at ScienceDirect

Chinese Chemical Letters

journal homepage: www.elsevier.com/locate/cclet

Nonmetallic phosphorus alloying to regulate the oxygen reduction mechanisms of platinum catalyst

Yizhe Chen[a,1], Yuzhou Jiao[b,1], Liangyu Sun[a,1], Cheng Yuan[a], Qian Shen[a], Peng Li[b,c], Shiming Zhang[a,c,*], Jiujun Zhang[a,*]

[a] Institute for Sustainable Energy/College of Sciences, Shanghai University, Shanghai 200444, China
[b] College of Chemistry and Molecular Sciences, Wuhan University, Wuhan 430072, China
[c] Key Laboratory of Advanced Energy Materials Chemistry (Ministry of Education), Nankai University, Tianjin 300071, China

ARTICLE INFO

Article history:
Received 12 November 2024
Revised 13 December 2024
Accepted 20 December 2024
Available online 21 December 2024

Keywords:
Proton exchange membrane fuel cells
Oxygen reduction electrocatalysis
Mechanism regulation
Phosphorus-alloying of Pt microwave synthesis

ABSTRACT

Platinum (Pt) nanoparticle catalysts remain the most popular cathode materials for oxygen reduction reaction (ORR) in proton exchange membrane fuel cells. Non-metallic alloying of Pt has become an emerging strategy to improve electrocatalytic performance, however, the electrocatalytic ORR mechanisms still need to be understood for further improvement toward practical application. Herein, a rapid microwave reduction method is employed for alloying phosphorous (P) into Pt to form a carbon supported phosphorus-alloyed Pt nanoparticle catalyst (P-Pt/C), which demonstrates the ability to replace commercial Pt/C. By a combination of density functional theory calculations and *in-situ* electrochemical Raman spectroscopy, the regulation role of P-alloying in the electrocatalytic mechanisms is revealed. It is found that the nearby Pt atoms can convert the ORR pathway from associative one to dissociative one, exhibiting a spontaneous dissociation of *OOH intermediate to *OH and *O species as well as a change of potential determining step to *O protonation. Furthermore, the strategy of large-scale economic synthesis of such alloying Pt-based catalyst is also established, demonstrated by a gram-level synthesis per batch. This study puts insight into the electrocatalytic ORR fundamentals of Pt-alloying with non-metals and provides a basis for the reasonable design and synthesis of efficient nonmetals-alloyed Pt catalysts.

Proton exchange membrane fuel cells (PEMFCs) using hydrogen as the fuel are a kind of energy conversion devices with high energy density, high conversion efficiency, and environmental friendliness [1–3]. The oxygen reduction reaction (ORR) at the cathode of a PEMFC is a key electrode reaction but with sluggish kinetics. To speed up ORR to a practical rate, some electrocatalysts with high activity and stability are needed [4–6]. To date, the most popular catalysts for ORR are still platinum (Pt)-based nanoparticle materials, which have low Pt nature abundance and are expensive [7–12]. Furthermore, the activity and stability of Pt-based electrocatalysts is still not high enough for long-term practical operation of the corresponding PEMFCs. Therefore, it is highly desirable to further increase the catalytic ORR activity and stability, and at the same to reduce the Pt loading and even replacing it by non-noble metals. Regarding improvement of catalyst activity and stability, developing innovative methodologies for synthesizing Pt-based materials is always the research hotspot. In general, the synthesis methods of Pt-based catalysts include microwave reduction [13,14], solvent-assisted thermal reduction [15–17], electrodeposition [18–20], atomic layer deposition [21,22], and impregnation reduction [23,24]. It has been found that microwave synthesis technology based on the microwave electrical heating principle can make more uniform Pt-based catalysts in size and morphology [25–27]. This method has the advantages of low energy consumption, fast heating rate, as well as efficient nucleation and crystallization of Pt nanoparticles.

Alloying Pt with other metals or non-metals to achieve high-performance Pt-based catalysts has also considered to be the innovative method in catalyst materials synthesis. The catalytic enhancement mechanisms through alloying have been discussed based on the d-band center theory, the strain and ligand effects, and the volcano principle. In general, Pt alloying can be accomplished by the introduction of transition metals (M = Mn, Fe, Co, Ni, Cu, *etc.*) and/or non-metals (X = B, C, N, P, S, *etc.*) into the Pt lattice to obtain the alloys of PtM and PtX [28–35]. The non-metals

* Corresponding authors.
E-mail addresses: smzhang@shu.edu.cn (S. Zhang), jiujun.zhang@i.shu.edu.cn (J. Zhang).
[1] These authors contributed equally to this work.

https://doi.org/10.1016/j.cclet.2024.110789
1001-8417/

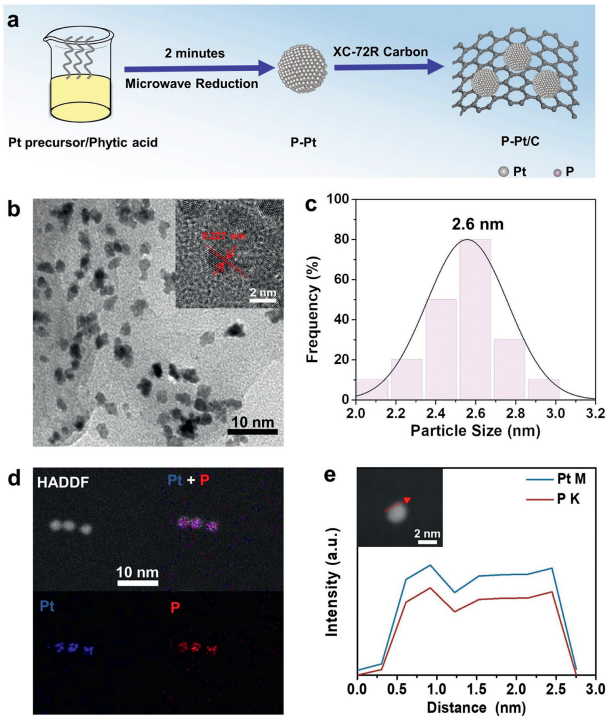

Fig. 1. (a) Schematic illustration for the preparation of P-Pt/C. (b) TEM and HRTEM (in the inset) images of P-Pt/C catalyst. (c) Particle size distribution of P-Pt nanoparticles. (d) HAADF-STEM and its elemental mapping images of P-Pt/C catalyst. (e) STEM-EDS line-scanning profile of an individual P-Pt nanoparticle.

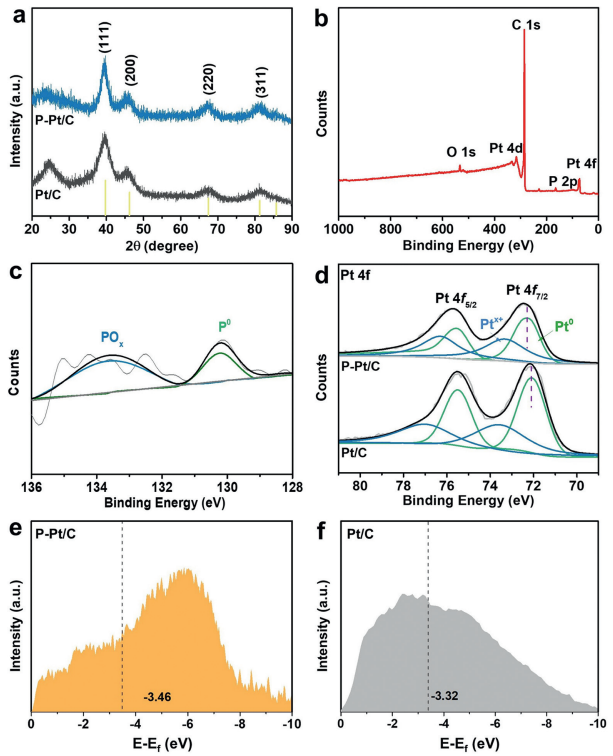

Fig. 2. (a) XRD patterns of P-Pt/C and Pt/C. (b) XPS survey spectrum of P-Pt/C. High-resolution XPS spectra of (c) P 2p and (d) Pt 4f. XPS valence band spectra for (e) P-Pt/C and (f) Pt/C.

alloying of Pt has gradually become the research spot due to the possible uniqueness in improving ORR electrocatalysis. Specially, the non-metallic elements with large electronegativity can strongly bind with Pt and greatly regulate its electronic properties. Even if the non-metal dissolves, the produced anions would not damage the components of PEMFCs. Although there has been some substantial progress of the nonmetals-alloyed Pt catalysts in recent years, there is still no enough studies and evidences for non-metallic alloying on enhancement mechanisms of catalytic ORR.

In this work, the catalyst system of carbon-supported P-alloyed Pt nanoparticles (P-Pt/C) is successfully synthesized by a simple microwave reduction method and the ORR mechanisms of such a P-alloyed Pt catalyst are deeply explored. The microwave reduction method can obtain about 2.6 nm of Pt nanoparticles through a rapid reaction process of 2 min to achieve the gram-scale synthesis of P-Pt/C catalyst. The resulting P-Pt/C exhibits higher electrocatalytic ORR performance than commercial Pt/C in both half-cells and H_2-O_2 PEMFCs. The results of experimental valence band spectra and theoretical calculations together demonstrate that the incorporation of P can downshift the d-band center of Pt and weaken the oxygen species adsorption on the Pt surface. By further combining with *in-situ* electrochemical Raman spectroscopy, it is found that the P-alloying can transform ORR pathway of Pt site near P from an associative mechanism to a dissociative mechanism with a significantly declined free-energy barrier of potential determining step.

Fig. 1a shows the synthesis flowchart of the P-Pt/C catalyst. Firstly, the Pt precursor and phytic acid are mixed thoroughly in an alkaline ethylene glycol solution. Subsequently, the microwave reduction of the above mixture solution is proceeded under the microwave power of 160 W at 160 °C for 2 min. The resulting P-Pt product is then supported on Vulcan XC-72R carbon black to obtain the final P-Pt/C catalyst. Fig. 1b shows the transmission electron microscopy (TEM) image of P-Pt/C. It can be seen that the prepared P-Pt nanoparticles are uniformly distributed on the surface of carbon black, with an average particle size of about 2.6 nm (Fig. 1c). Also, we analyze the morphology and size of microwave-synthesized Pt nanoparticles (Fig. S1 in Supporting information). The results show that the average size of Pt nanoparticles with a uniform dispersion is 2.8 nm. This phenomenon indicates that P-alloying can slightly reduce the size of Pt nanoparticles. Smaller particle sizes can provide a larger surface area, which contributes to the improvement of ORR performance [36]. The high-resolution TEM (HRTEM) image in the inset of Fig. 1b shows a Pt(111) lattice spacing of 0.227 nm, the same as that of Pt/C (Fig. S2 in Supporting information). Further observations by high angle annular dark field scanning TEM (HAADF-STEM) and the corresponding elemental mapping images (Fig. 1d) reveal that both elements of Pt and P are uniformly distributed throughout the P-Pt nanoparticles. Fig. 1e shows the line-scanning profile of an individual P-Pt, also indicating the homogeneous alloying of Pt and P. In addition, the gram-scale synthesis of P-Pt/C catalyst has been successfully achieved through this facile microwave method (Fig. S3 in Supporting information).

Fig. 2a exhibits the XRD patterns of P-Pt/C and Pt/C. The introduction of P does not shift the characteristic peaks of Pt. The diffraction peaks of P-Pt/C and Pt/C at $2\theta = 39.85°$, 46.22°, 67.59°, 81.52°, and 85.89° correspond to the (111), (200), (220), (311), and (222) planes of the face-centered cubic crystal structure, respectively. This observation can be attributed to the low incorporation of P and the similar atomic radius between Pt and P, which do not manifest as peak shifts in the XRD patterns. The chemical composition and electronic structure of the two catalysts can be analyzed by X-ray photoelectron spectroscopy (XPS). The signals of Pt, P, C, and O can be seen in the survey spectrum of P-Pt/C (Fig. 2b). The P:Pt atomic ratio provided by XPS analysis is about 1:14.6, while one obtained by ICP-OES test is about 1:17.1, suggesting that the P element is uniformly distributed in the P-Pt/C catalyst. The high-

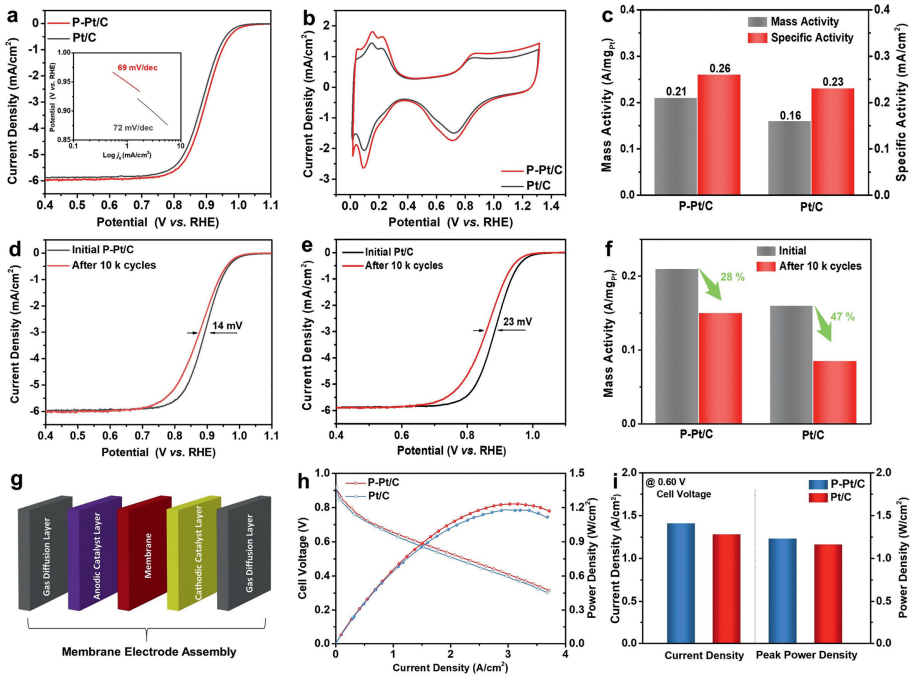

Fig. 3. (a) ORR polarization curves and the corresponding Tafel plots and slopes in the inset, (b) CV curves, and (c) mass activities and specific activities at 0.9 V (*vs.* RHE) for P-Pt/C and commercial Pt/C. ORR polarization curves of (d) P-Pt/C and (e) commercial Pt/C before and after 10 k cycles between 0.6 V and 1.1 V (*vs.* RHE), and (f) the corresponding mass activity changes of P-Pt/C and Pt/C. (g) Schematic diagram of membrane electrode assembly. (h) *I-V* polarization and power density curves, and (i) histograms of current densities at a cell voltage of 0.6 V and maximum power densities of P-Pt/C and Pt/C (Cathode loading: 0.1 mg_{Pt}/cm^2; Test conditions: 80 °C, 100% RH, 100 kPa absolute pressure).

resolution P 2p XPS spectrum (Fig. 2c) shows that the elemental state (P^0) exists at about 130.2 eV, and the oxidized state (PO_x) is at about 133.6 eV. Fig. 2d shows the Pt 4f XPS spectra of P-Pt/C and Pt/C with two characteristic peaks of Pt $4f_{7/2}$ and Pt $4f_{5/2}$, fitted by the metallic (Pt^0) and oxydic (Pt^{x+}) states. As marked by the dotted lines, there is a positive shift of 0.2 eV for P-Pt/C compared to Pt/C. This phenomenon can be attributed to the partial electron transfer from Pt to P because of the difference in electronegativity between Pt and P. From the results of XPS valence band spectra (Figs. 2e and f), the d-band center of P-Pt/C is lower than that of Pt/C. The declined d-band center can lead to the weak adsorption of oxygen species on the Pt surface, thus facilitating the ORR kinetics [37,38].

In order to obtain the best performance P-Pt/C catalyst, different synthesis conditions were optimized in this work. The effects of Pt:P atomic ratios (Fig. S4 in Supporting information), times (Fig. S5 in Supporting information), temperatures (Fig. S6 in Supporting information), and microwave powers (Fig. S7 in Supporting information) on catalyst performance were investigated. An optimal P-Pt/C catalyst can be obtained at the Pt:P ratio of 1:2, time of 120 s, temperature of 160 °C, and microwave power of 160 W. As shown by the ORR polarization curves in Fig. 3a, the half-wave potential ($E_{1/2}$) of P-Pt/C is 0.894 V (*vs.* RHE), which positively shifts by about 12 mV compared to that of commercial Pt/C (0.882 V). The inset in Fig. 3a further illustrates Tafel plots and the corresponding slope values. The Tafel slope of P-Pt/C is 69 mV/dec, lower than that of Pt/C (72 mV/dec). The cyclic voltammetry (CV) curves are shown in Fig. 3b, from which the electrochemical active surface area (ECSA) values are calculated to be 80.52 m^2/g_{Pt} and 68.37 m^2/g_{Pt} for P-Pt/C and Pt/C, respectively (Fig. S8 in Supporting information). The larger ECSA value for P-Pt/C is mainly due to the smaller nanoparticle size (~2.6 nm), implying that there are more exposed active sites for catalyzing the ORR. Furthermore, the excellent ORR performance of P-Pt/C can be demonstrated by comparing the mass and specific activities of two catalysts (Fig. 3c) at the potential of 0.9 V (*vs.* RHE). The P-Pt/C catalyst shows mass activity of 0.21 A/mg_{Pt} and specific activity of 0.26 mA/cm^2, superior to those of Pt/C catalyst (0.16 A/mg_{Pt} and 0.23 mA/cm^2). These results suggest that P-alloying has an enhancement effect on ORR kinetics. In addition, the electrochemical stability of P-Pt/C and Pt/C were further evaluated by accelerated durability tests (ADTs) through 10,000 potential cycles between 0.6 V and 1.1 V. After the ADTs, the $E_{1/2}$ of P-Pt/C was reduced to 0.880 V, a decrease of 14 mV (Fig. 3d). In contrast, the loss of Pt/C was greater, with the $E_{1/2}$ decreasing from 0.882 V to 0.859 V, a downward shift of 23 mV (Fig. 3e). As depicted in Fig. 3f, the mass activity of P-Pt/C decreased by only 28%, whereas that of Pt/C dropped by 47%.

The electrocatalytic performance of P-Pt/C was evaluated as a cathode catalyst (Pt loading of 0.1 mg_{Pt}/cm^2) in H_2-O_2 PEMFCs with commercial Pt/C as the reference. The schematic membrane electrode assembly is shown in Fig. 3g. From the typical current-voltage (*I-V*) polarization and power density curves in Fig. 3h, it can be seen that the P-Pt/C possesses higher current density and power density than those of Pt/C, respectively. As shown in Fig. 3i, the current density at 0.6 V and the maximum power density (P_{max}) for P-Pt/C is 1.41 A/cm^2 and 1.23 W/cm^2, respectively, which are higher than those of Pt/C (1.28 A/cm^2 and 1.16 W/cm^2). These H_2-O_2 fuel cell test results indicate that P-Pt/C is an efficient ORR electrocatalyst for practical application in PEMFCs.

Density functional theory (DFT) calculations were further performed to understand the mechanism of P-alloying on ORR activity improvement of Pt catalyst. The Pt(111) model was constructed as a $4 \times 4 \times 3$ slab. For constructing the P-Pt(111) model, one Pt atom on the Pt(111) surface was replaced with a P atom. The ORR pathways on these two catalysts are illustrated in Fig. 4a. For the reaction on Pt (the top of Fig. 4a), the O_2 molecule tends to be adsorbed in a top-bridge-top configuration to convert into stable *OOH intermediate after protonation, thus the ORR is proceeded *via* an associative mechanism. The incorporation of P atom can produce two different types of Pt sites. When the ORR occurs on Pt

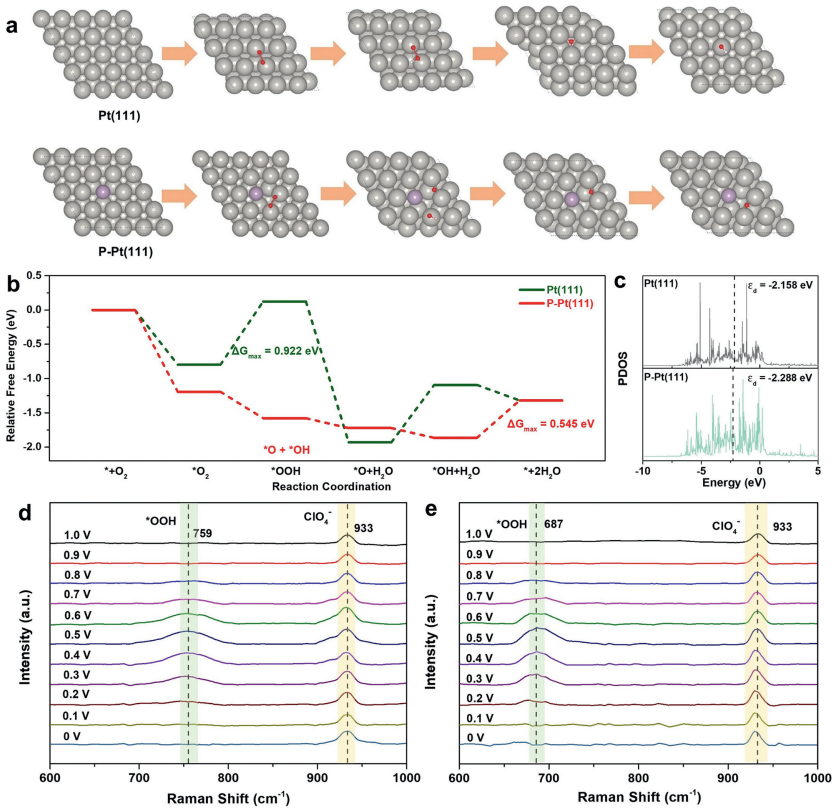

Fig. 4. (a) Configuration models adsorbed with oxygen intermediates at different reaction steps, (b) free energy paths of the ORR at 0.9 V (*vs.* RHE), and (c) projected density of states (PDOS) of the surface Pt atoms in Pt(111) and P-Pt(111). *In-situ* electrochemical Raman spectra of (d) Pt/C and (e) P-Pt/C in O_2-saturated 0.1 mol/L $HClO_4$ solution.

atoms far from the P atom, the reaction mechanism is consistent with Pt(111) (Fig. S9 in Supporting information). It is worth noticing that when ORR occurs on Pt atoms surrounding P, its mechanism transforms to the dissociative mechanism (the bottom of Fig. 4a). The protonated $*O_2$ spontaneously cleaves into one *O at the bridge site and a *OH species at the apex site.

The free energy pathway diagram, as shown in Fig. 4b, indicates that the potential determining step (PDS) for ORR on Pt(111) is the protonation of $*O_2$, with a free energy barrier as high as 0.922 eV. However, the protonation of $*O_2$ on Pt sites surrounding the P atom changes from a strongly endothermic step to a spontaneous step. The PDS shifts to the protonation of *O with a free energy barrier of only 0.545 eV, greatly lower than that of Pt(111). Moreover, when the ORR occurs on Pt atoms far from the P atom, as shown in Fig. S10 (Supporting information), the PDS reaction barrier of 0.920 eV is almost identical to that of Pt(111) along the same ORR associative pathway. This result suggests that the P-alloying can make ORR mechanism transformation on Pt sites near P, meanwhile significantly accelerating catalytic ORR kinetics. Fig. 4c reveals the projected density of states (PDOS) and d-band center (ε_d) values of surface Pt atoms in Pt(111) and P-Pt(111). Importantly, the P-alloying can lower d-band center, indicating a weakening of adsorption capability of oxygenated species, thereby improving catalytic ORR activity.

Furthermore, the *in-situ* electrochemical Raman technique was used to understand the ORR mechanism of P-alloying on Pt from molecular level perspective. As shown in Figs. 4d and e, Pt/C and P-Pt/C show a characteristic peak at the same position of 933 cm^{-1}, corresponding to the response of ClO_4^- in the electrolyte. In addition, when the potential is reduced to 0.8 V, there is a distinct peak at about 759 cm^{-1} for Pt/C (Fig. 4d). According to previous studies [39,40], this peak should be ascribed to the O–O stretching vibration of *OOH intermediate. In contrast, this characteristic peak appears at 687 cm^{-1} for P-Pt/C (Fig. 4e), which is redshifted by 72 cm^{-1} relative to Pt/C. The lower wavenumber suggests that the O–O bonds in *O–OH could be of lower energy and more likely to break [41,42], indicating that the produced *O–OH during the process of $*O_2$ protonation for P-Pt/C would be more easily cleaved.

In summary, a facile microwave reduction method with a reaction time of only 2 min is successfully developed in this work for large-scale synthesis of the P-alloyed Pt nanoparticle catalyst. The average particle size of the synthesized P-Pt nanoparticles is about 2.6 nm. Combined with the results of XPS valence spectra and DFT calculations, it can be found that P-alloying moves down the d-band center of Pt. A combination of theoretical calculations and *in-situ* electrochemical Raman spectroscopy reveals the manipulation of P-alloying on ORR mechanism by a shift of reaction pathway from associative to dissociative. The alloying of Pt with P can result in the spontaneous dissociation of *OOH intermediates into *O and *OH species and the transformation of potential determining step to the protonation of *O with a significantly reduced free-energy barrier. As a result, P-Pt/C shows superior activity and stability to Pt/C. In H_2-O_2 PEMFC, the maximum power density of P-Pt/C can be up to 1.23 W/cm^2, higher than that of Pt/C. This study presents a facile microwave method for the large-scale synthesis of P-alloyed Pt nanoparticle catalyst and a systematic insight into the ORR mechanism for advancing the non-metallic alloying of Pt-based catalysts.

Declaration of competing interest

The authors declare that they have no known competing financial interests or personal relationships that could have appeared to influence the work reported in this paper.

CRediT authorship contribution statement

Yizhe Chen: Writing – review & editing, Writing – original draft, Methodology, Data curation. **Yuzhou Jiao:** Data curation. **Liangyu Sun:** Data curation. **Cheng Yuan:** Formal analysis. **Qian Shen:** Data curation. **Peng Li:** Data curation. **Shiming Zhang:** Writing – review & editing, Methodology, Funding acquisition. **Jiujun Zhang:** Writing – review & editing.

Acknowledgments

This work was sponsored by the Natural Science Foundation of Shanghai (No. 23ZR1423900) and the National Natural Science Foundation of China (No. 22272105). The authors would like to thank Shiyanjia Lab (www.shiyanjia.com) for the TEM analysis.

Supplementary materials

Supplementary material associated with this article can be found, in the online version, at doi:10.1016/j.cclet.2024.110789.

References

[1] M. Chen, J. Chen, C. Jia, et al., Cell Rep. Phys. Sci. 4 (2023) 101204.
[2] Y. Chen, S. Zhang, J. Jung, J. Zhang, Prog. Energy Combust. Sci. 98 (2023) 101101.
[3] Z. Yang, Y. Chen, S. Zhang, J. Zhang, Adv. Funct. Mater. 33 (2023) 2215185.
[4] G. Fisseha, Y. Hu, Y. Yu, et al., Chin. Chem. Lett. 35 (2024) 108445.
[5] S. Zhang, M. Chen, X. Zhao, et al., Electrochem. Energy Rev. 4 (2021) 336–381.
[6] L. Liu, X. Rao, S. Zhang, J. Zhang, Chem 10 (2024) 1994–2030.
[7] C. Zhang, Q. Zhang, Y. Hu, et al., Chin. Chem. Lett. 36 (2025) 110429.
[8] Q. Meyer, C. Yang, Y. Cheng, C. Zhao, Electrochem. Energy Rev. 6 (2023) 16.
[9] J. Huang, L. Sementa, Z. Liu, et al., Nat. Catal. 5 (2022) 513–523.
[10] C. Yuan, S. Zhang, J. Zhang, Front. Energy 18 (2024) 206–222.
[11] X. Liu, G. Wu, Q. Li, eScience (2024), doi:10.1016/j.esci.2024.100270.
[12] J. Liang, S. Li, X. Liu, et al., Nat. Catal. 7 (2024) 719–732.
[13] J. Cai, J. Chen, Y. Chen, J. Zhang, S. Zhang, iScience 26 (2023) 106730.
[14] J. Cai, Y. Chen, R. Zhang, et al., Chin. Chem. Lett. 36 (2025) 110255.
[15] D. Xue, Y. Yuan, Y. Yu, et al., Nat. Commun. 15 (2024) 5990.
[16] Y. Liao, J. Li, S. Zhang, S. Chen, Chin. J. Catal. 42 (2021) 1108–1116.
[17] X. Liu, Y. Wang, J. Liang, et al., J. Am. Chem. Soc. 146 (2024) 2033–2042.
[18] J. Kim, H. Kim, G. Han, et al., Exploration 2 (2022) 20210077.
[19] B. Geboes, J. Ustarroz, K. Sentosun, et al., ACS Catal. 6 (2016) 5856–5864.
[20] Q. Hua, X. Chen, J. Chen, et al., ACS Catal. 14 (2024) 7526–7535.
[21] W. Lee, S. Bera, H. Woo, et al., Chem. Eng. J. 442 (2022) 136123.
[22] G. Liccardo, M.C. Cendejas, S.C. Mandal, et al., J. Am. Chem. Soc. 146 (2024) 23909–23922.
[23] B. Liu, R. Feng, M. Busch, et al., ACS Nano 16 (2022) 14121–14133.
[24] W. Zhu, Y. Pei, H. Liu, et al., Adv. Sci. 10 (2023) 2206062.
[25] J. Quinson, M. Inaba, S. Neumann, et al., ACS Catal. 8 (2018) 6627–6635.
[26] Z. Wu, P. Yang, Q. Li, et al., Angew. Chem. Int. Ed. 62 (2023) e202300406.
[27] W.Y. Noh, J. Mun, Y. Lee, et al., ACS Catal. 12 (2022) 7994–8006.
[28] M. Zhou, C. Li, J. Fang, Chem. Rev. 121 (2021) 736–795.
[29] N. Alonso-Vante, Electrochem. Energy Rev. 6 (2023) 3.
[30] C. Ahn, J.E. Park, S. Kim, et al., Chem. Rev. 121 (2021) 15075–15140.
[31] K. Wang, J. Huang, H. Chen, et al., Electrochem. Energy Rev. 5 (2022) 17.
[32] L. Ding, A. Wang, G. Li, et al., J. Am. Chem. Soc. 134 (2012) 5730–5733.
[33] Y. Chen, R. Zhang, L. Sun, S. Zhang, J. Zhang, Chem. Eng. J. 485 (2024) 149998.
[34] L. Hui, D. Yan, X. Zhang, et al., Angew. Chem. Int. Ed. 63 (2024) e202410413.
[35] L. Sun, Y. Chen, R. Zhang, S. Zhang, J. Alloys Compd. 985 (2024) 173988.
[36] H. Cheng, R. Gui, H. Yu, et al., Proc. Natl. Acad. Sci. U. S. A. 118 (2021) e2104026118.
[37] B. Lu, L. Shen, J. Liu, et al., ACS Catal. 11 (2021) 355–363.
[38] K. Guo, D. Fan, J. Bao, Y. Li, D. Xu, Adv. Funct. Mater. 32 (2022) 2208057.
[39] J. Dong, X. Zhang, V. Briega-Martos, et al., Nat. Energy 4 (2019) 60–67.
[40] K. Wang, H. Yang, Q. Wang, et al., Adv. Energy Mater. 13 (2023) 2204371.
[41] H. Zhong, H. Ze, X. Zhang, et al., ACS Catal. 13 (2023) 6781–6786.
[42] H. Ze, X. Chen, X. Wang, et al., J. Am. Chem. Soc. 143 (2021) 1318–1322.